Supporting Information: Exciton Condensation in an Atomically-thin MoS_2 Semiconductor

Andrés Granados del Águila,[1†*] Yi Ren Wong,[1†] Xue Liu[2], Antonio Fieramosca[1], T. Thu Ha Do[1], Marco Battiato[1], Qihua Xiong[3,4*]

[1]*Division of Physics and Applied Physics, School of Physical and Mathematical Sciences, Nanyang Technological University, 637371, Singapore.*

[2]*Institutes of Physical Science and Information Technology, Anhui University, Hefei, China.*

[3]*Beijing Innovation Center for Future Chips, Tsinghua University, Beijing 100084, China.*

[4]*Beijing Academy of Quantum Information Sciences, Beijing 100193, China.*

[†] *These authors contributed equally to this work.*

[*] *To whom correspondence should be addressed:*

qihua_xiong@tsinghua.edu.cn ; a.granadosdelaguila@ntu.edu.sg

This PDF file includes:

Materials and Methods
Supplementary Text
Figs. S1 to S18

1 Materials and Methods

A. Device Fabrication Large MoS_2 monolayers with the typical long side of 40 to 60 μm and area of $\sim$1200 μm^2 were mechanically exfoliated from natural bulk MoS_2 crystals onto a polydimethylsiloxane (PDMS) stamp. The MoS_2 monolayers were then carefully transferred from the PDMS stamp onto clean 285 nm SiO_2/Si p-type dry oxide substrates, ensuring that smooth, uncracked large area monolayers are obtained upon transfer. The successful transfers were verified under an optical microscope by optical contrast. A poly(methyl methacrylate) (PMMA) mask was spin coated on the substrates and patterned electrical contact areas were defined on the mask by standard electron beam lithography. 5 nm Cr/ 50 nm Au electrical contacts were subsequently deposited by thermal evaporation. The final devices were obtained after an acetone lift-off procedure. To control the electron concentration of the MoS_2 devices in our optical experiments, a backgate voltage was applied to the Si substrate and the MoS_2 monolayers grounded via the electrical contacts.

B. Experimental Setup The fabricated devices were mounted on a cold finger cryostat and cooled down using a continuous flow of liquid helium. The cryostat station was mounted on the photoluminescence (PL) and transient reflectance (TR) imaging setup that operated in two different imaging configurations, as shown in Fig. 1.

In the PL imaging configuration, the samples were excited with a He-Ne (632.8 nm) continuous wave (cw) laser cleaned by an interference filter resonant with the *A*-exciton of the MoS_2 monolayer. Using a 50$\times$ objective lens (NA = 0.55), the laser was focused to locally excite a small spot with diameter of 1.5 μm on the large sample (see Fig. 2). The objective then collected the PL emission. An ultra-steep-edge long pass filter placed in the detection path before the optical detector removes reflected laser light, allowing only PL image signal to be measured. A set of lenses were added in the detection path to change the image magnification and effective field of view on the optical detector (sCMOS sensor). This enables imaging to be optimized for samples of different sizes. The sCMOS chip has an area of 2300 $\times$ 2300 pixels, 6.5 μm each. Our detection system provides a high spatial resolution of 40 nm per pixel in either axial direction.

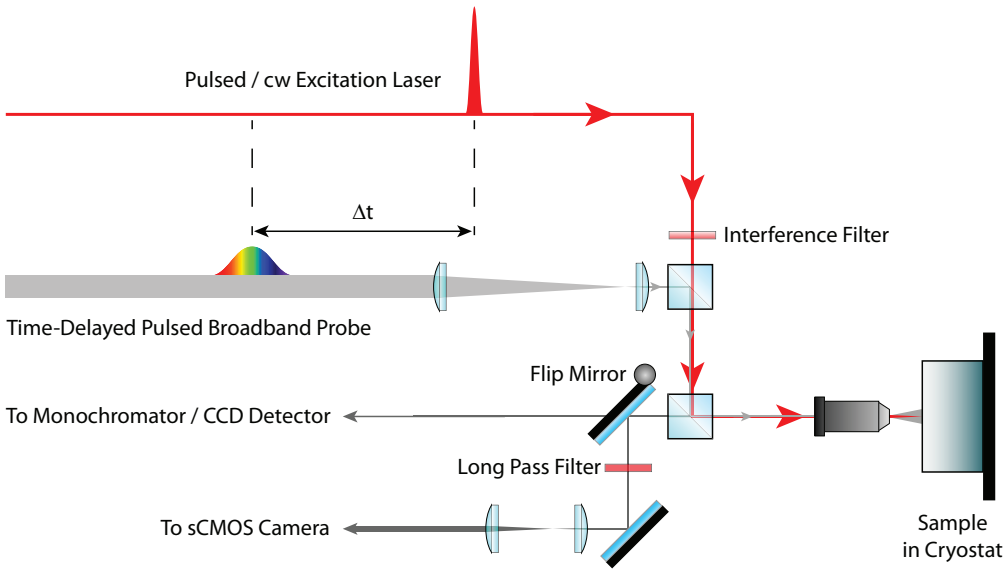

Fig. S1: PL Imaging and Spatiotemporally resolved TR spectroscopy experimental setup.

For TR imaging, a femtosecond pulsed pump laser (615 nm) is used to excite the sample. A pulsed broadband white light beam given a time delay Δt with respect to the pump is used to probe the changes in the reflectance of the sample in the visible (625 – 700 nm) region. The size of the probe beam illuminating the sample surface is controlled by a series of lenses, which focuses the probe at the back focal plane of the objective lens to maximize the probe and cover the entire sample. The reflected probe beam was collected by the same objective and dispersed by a single grating (600 gr/mm) monochromator with 550 mm of focal length and the signal was detected by a scientific CCD detector cooled with liquid-nitrogen. Energy-space reflectance spectrum map images are measured for each time delay under pump on/off conditions.

C. Sample Characterization We first characterized the fabricated devices by measuring its spatially-resolved reflectance spectrum as a function of the back-gate voltage. The spatially-resolved reflectance contrast profile is calculated by using the expression given as

$$RC(x,E) = \frac{R_{\text{Sample}}(x,E) - R_{\text{Substrate}}(x,E)}{R_{\text{Substrate}}(x,E)} \tag{1}$$

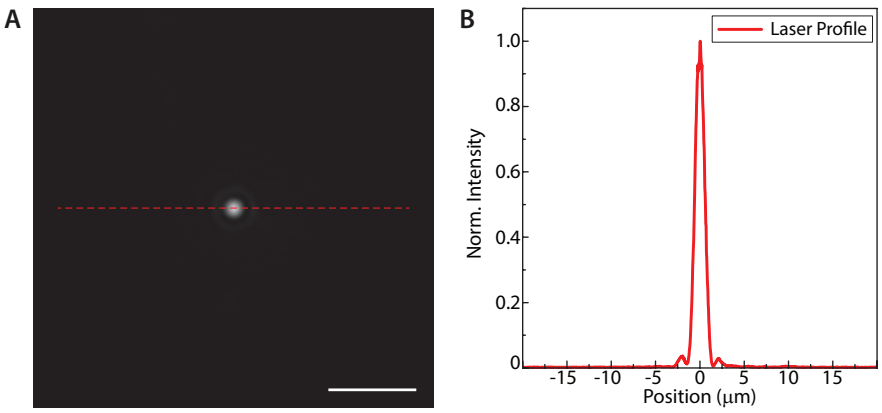

Fig. S2: Excitation laser profile. (**A**) Laser beam profile as seen in real space on the sCMOS camera (scale bar: 10 μm). (**B**) Cross-section normalized intensity profile of the laser extracted from the image in **(A)** (red-dotted line). The full width at half maximum (fwhm) of the laser spot is σ_{Laser} = 1.5 μm .

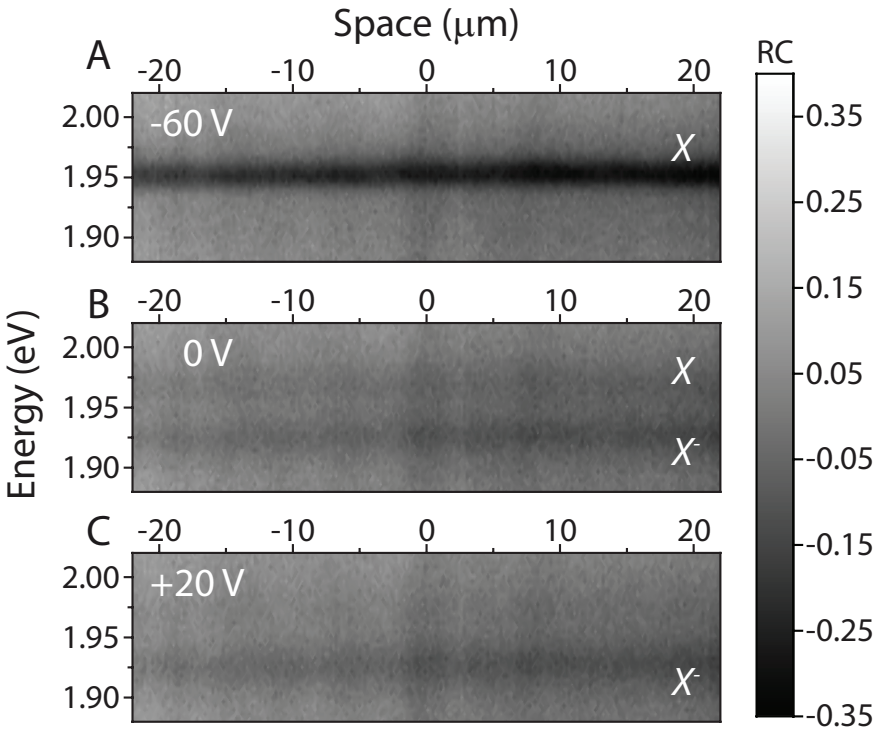

Fig. S3: Spatially-resolved reflectance contrast spectroscopy measurements. Spatially-resolved reflectance contrast for **(A)** V_g = -60 V, **(B)** V_g = 0 V and **(C)** V_g = +20 V. In all $RC(X, E)$ images, neutral (X) and charge (X^-) excitons exhibit a constant energy over the length of the MoS_2 sample probed that reveals the homogeneity of our high-quality monolayer devices.

Our high-quality devices exhibit homogeneous reflectance contrast spatial profiles as shown in Fig. 3. Sample inhomogeneities, such as spatial domains with higher doping concentration would be observed as changes in the intensity and spectral position of the excitonic resonance over the length of the MoS_2 sample probed.

2 Supplementary Text

A.1 PL Imaging with edge excitation We have investigated the long-range transport in the sample presented in the main text, denoted here as M1, by exciting the sample at different locations (at the center Figs. 4(A)-(C)) and at the edge Figs. 4(D)-(F)). With varying V_g and regardless of the excitation positioning, we observe a sample brightening with a homogeneous PL emission profile and long-range propagation. Particularly remarkable is the profile obtained when V_g = -60 V and exciting at one edge of the sample (Fig. 4(F)) that shows that the exciton propagation distance is limited by the sample size $\sim 50\mu$m.

A.2 Long-range transport reproducibility across multiple MoS_2 devices The superradiance PL with a strong dependence on V_g has been systematically reproduced in several large area MoS_2 monolayer devices, demonstrating that long-range propagation of excitons is a intrinsic feature of monolayer MoS_2. Figures 5(A)-(C) show the bright-field images for other devices, labelled as M2, M3 and M4, respectively, where the monolayer dimensions of up to 60 μm can be appreciated (see dashed lines). PL images at V_g = 0 V in Figs. 5(D)-(F) and at V_g = –60 V in Figs. 5(G)-(I) are shown for devices M2, M3 and M4, respectively.

All samples display a similar PL brightening and long-range spreading from the excitation spot when V_g is tuned to V_g = -60 V. It is noted that the 'turn-on' backgate voltage for the sudden PL brightening depends on the intrinsic doping level of each sample. Furthermore, since the doping level may vary across the sample, the PL images would present spatial inhomogeneities. Specifically, electron rich areas would be darker than others with a lower electron density. We believe that the use of local gates will be an efficient tool for manipulation of exciton flows and in the design of exciton circuits.

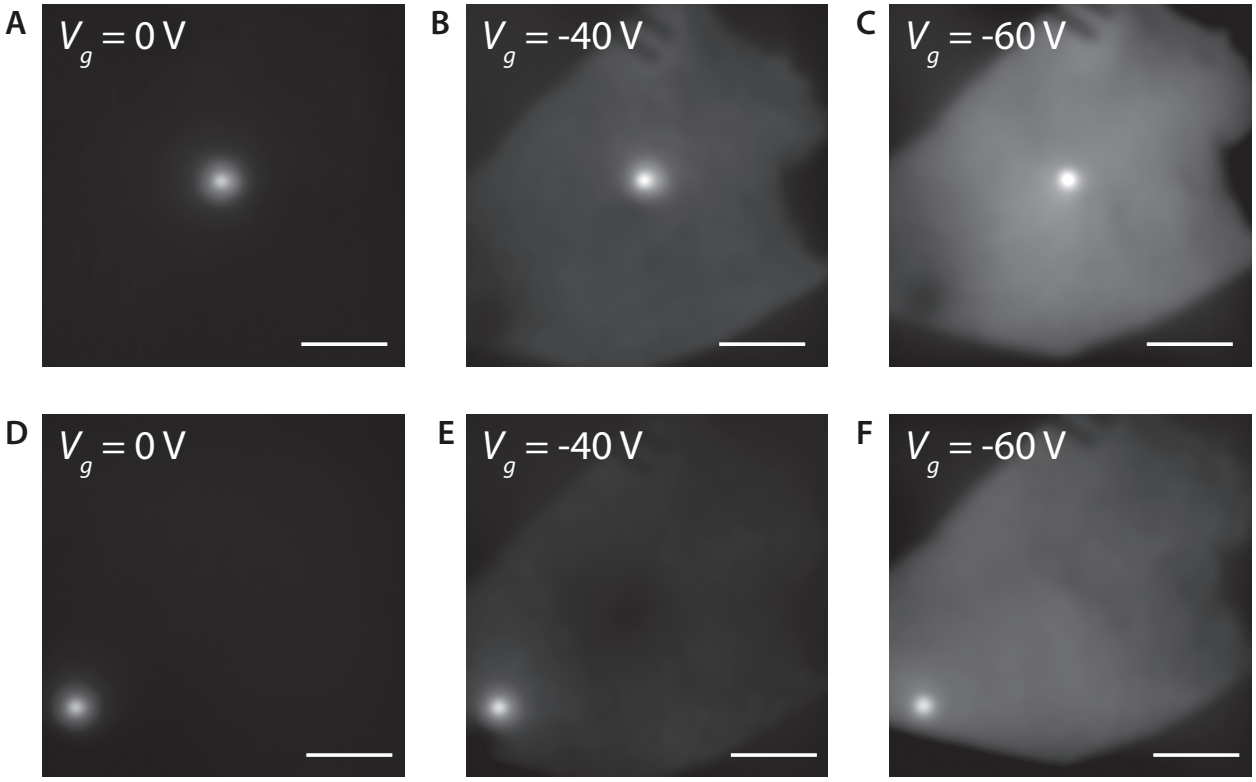

Fig. S4: PL emission comparing center and edge excitation. (**A–C**) PL emission from sample M1, which is presented in the main text, at $V_g = 0$ V, -40 V and -60 V respectively, when the cw laser is positioned at the center and (**D–F**) at the edge of the sample. All scale bars denote 10 μm.

A.3 Power and Temperature dependence To construct the full phase diagram for the gas to liquid transition in monolayer MoS_2 presented in the main text Fig. 2(D), the PL emission profiles were obtained as a function of backgate voltage, temperature and excitation power. At a fixed temperature, the laser excitation power was gradually increased from 10 μW to a maximum of 1000 μW. At each power value, the backgate voltage (V_g) was swept from +60 V to -60 V to obtain the backgate dependence of the MoS_2 PL emission. In this case, negative V_g corresponds to a low electron density ($i.e.$, a more insulating sample), while positive V_g corresponds to a high electron density ($i.e.$, a more conductive sample). This is repeated for temperatures from 20 K up to 250 K.

Figures 6(A)-(D) show a power-sweep PL experiments at fixed conditions of temperature T = 20 K and V_g = -60 V, while Fig. 6(E)-(H) show a temperature-sweep PL experiments at fixed conditions of excitation power P = 1000 μW and V_g = -60 V. Each PL image in Fig. 6 has been normalized by the integration

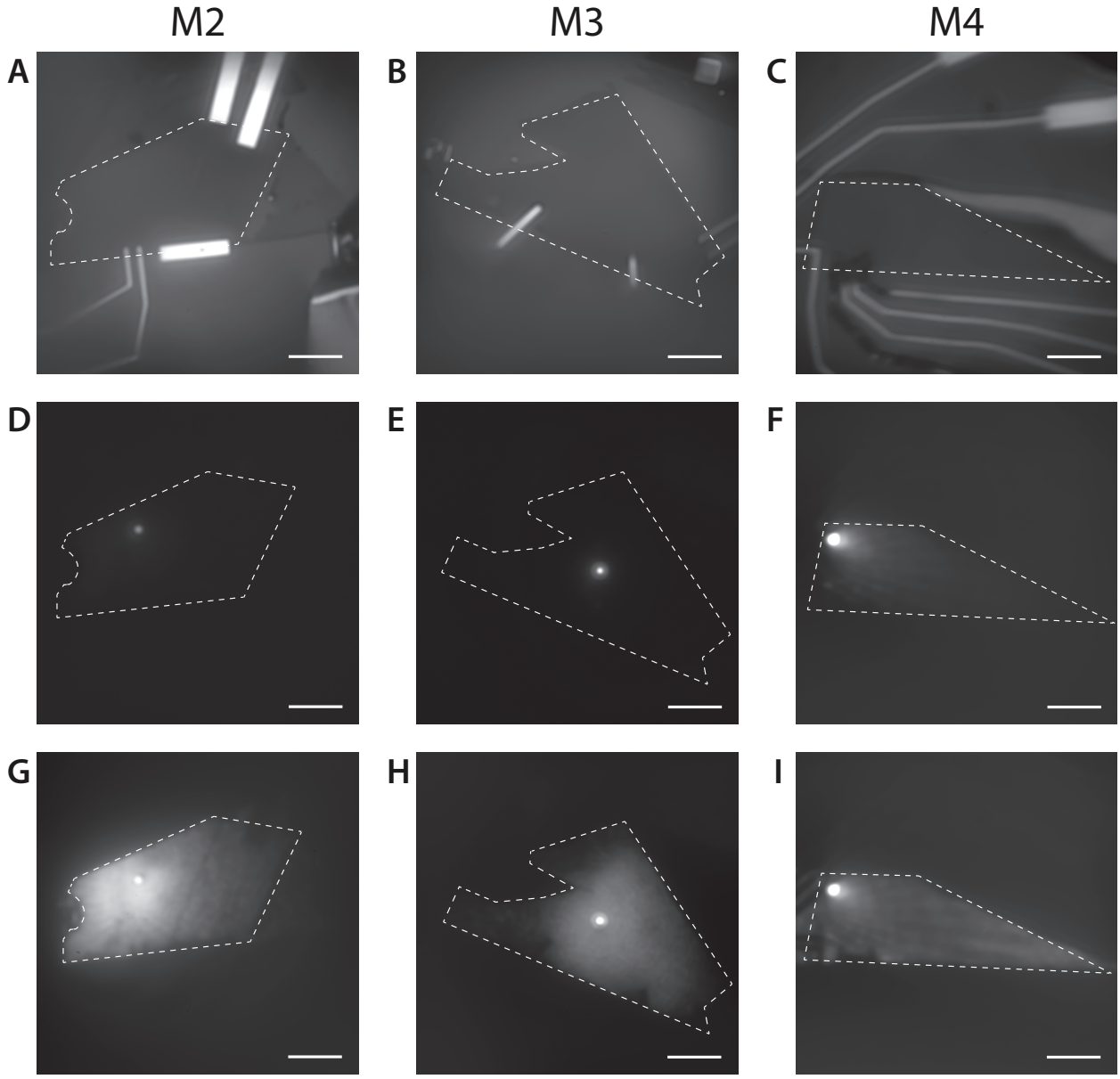

Fig. S5: Gate-dependent PL images in multiple MoS_2 monolayer devices. (**A–C**) Optical images of MoS_2 devices M2, M3 and M4 respectively. Dashed lines indicate the sample boundaries. Real space PL image profiles of M2, M3 and M4 at (**D–F**) $V_g = 0$ V and (**G –I**) $V_g =$ -60 V. All scale bars denote 10 μm.

time of the image, and to the maximum intensity defined by the central PL spot. The liquid phase is discernible from the gas phase by the emerging homogeneous sample-wide PL emission intensity. The liquid phase is present at even the lowest power conditions, which is in excellent agreement with theory of exciton conden-

sation [1] (see Section C for theoretical details). The transition temperature occurs at approximately 150 K as mentioned in the main text.

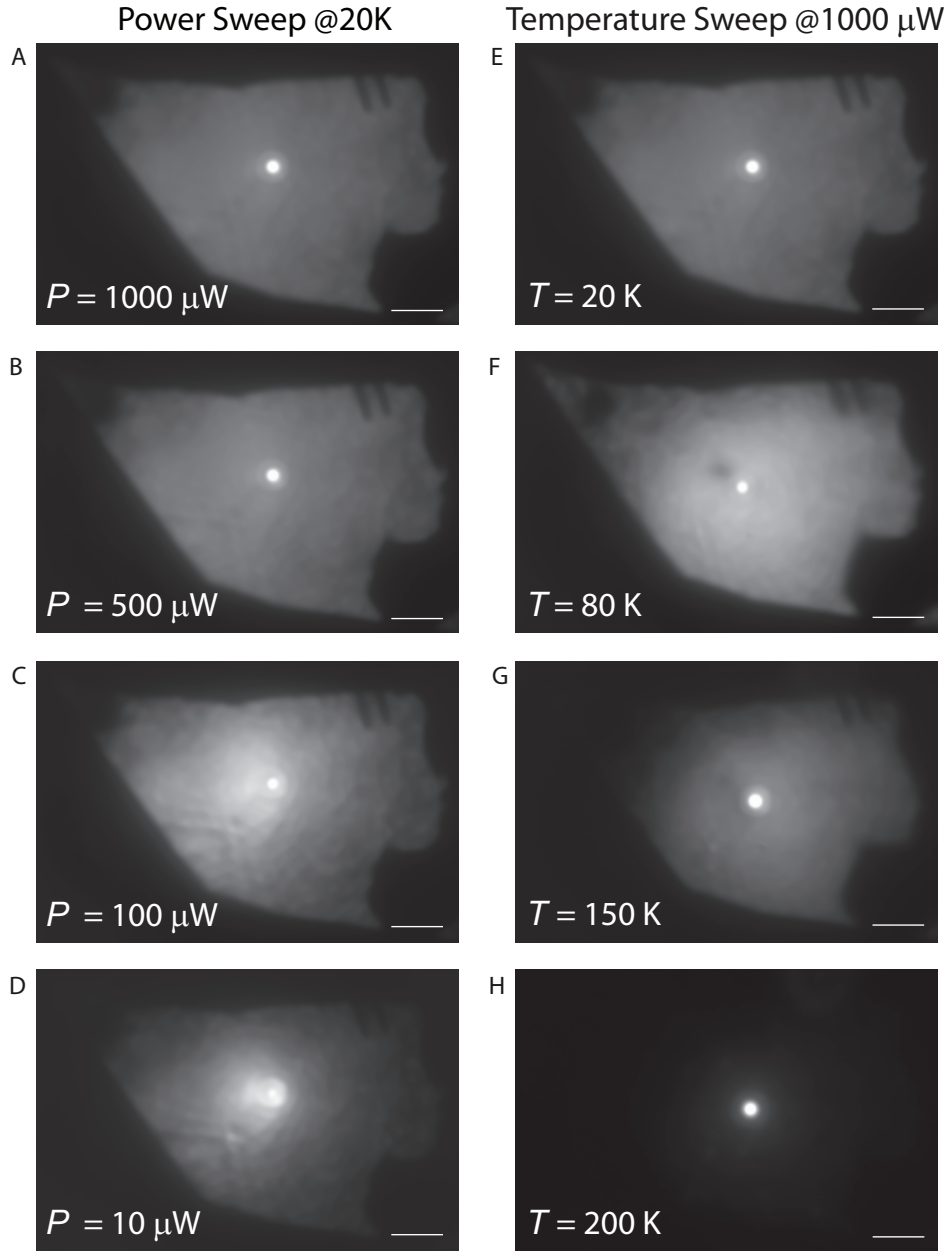

Fig. S6: Power and temperature dependent PL images. Real space PL images taken with V_g = –60 V at (**A–D**) fixed temperature of T = 20 K and varying power P = 1000, 500, 100 and 10 μW, respectively and (**E–H**) fixed power of P = 1000 μW for varying temperature T = 20 K, 80 K, 150 K and 200 K, respectively. All scale bars denote 10 μm.

B. PL Imaging Analysis

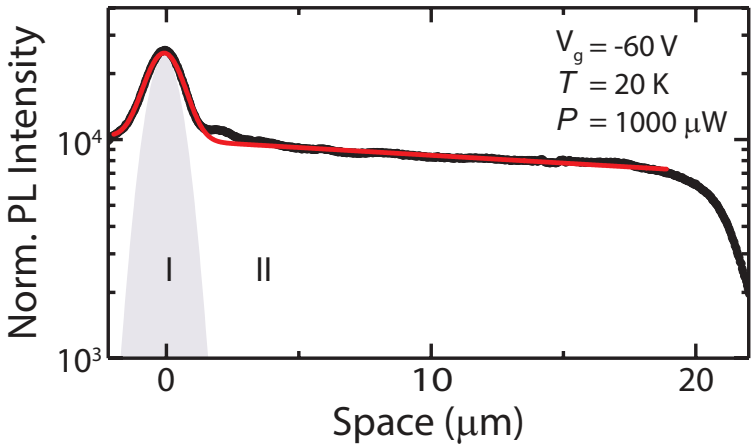

Fig. S7: PL Cross Section Analysis. Spatial cross-section profile (black dots) in a semi-logarithmic scale of the photoluminescence image taken at V_g= -60 V, P = 1000 μW and T = 20 K. Regions I (Gaussian) and II (exponential) of the bimodal PL distribution are indicated. The sharp drop of the PL intensity at $x \approx 20$ μm is due to the edge of the monolayer sample. The red solid-line is a fitting to the data by using Eq. (2). The laser position is taken as the zero.

B.1 Bimodal fitting of PL cross-sections: Obtaining transport length L_X The phase diagram constructed in the main text Fig. 2(D) based on the exciton transport length (L_X) is obtained by performing a detailed lineshape analysis of the cross sections of the PL images. At each V_g, P and T, the cross sections of the PL images have been systematically analyzed by a bimodal distribution given as

$$\mathrm{PL}(x) = y_o + Ae^{(\mathrm{x}-\mathrm{x_o})^2/2\sigma_\mathrm{I}'^2} + Be^{-(x-x_o)/L_X}, \tag{2}$$

where y_o is a PL background signal, x_o corresponds to the position of the laser on the sample, A and σ_I' correspond to the amplitude and standard deviation of the Gaussian distribution of the PL emission in region I. Thus, in region I, the gas transport length l_X^I is proportional to σ_I' ($l_X^I \propto \sigma_I'$). The third term in Eq. (2) accounts for the PL component at region II, which extends far beyond region I. The parameter B and the transport length of the exciton liquid L_X correspond to the amplitude and decay length, respectively, of the exponential distribution of the PL emission.

A typical fitting example of the PL cross section by using Eq. (2) is shown in Fig. 7, where we observe an excellent agreement. For a higher fitting accuracy of L_X, all PL spectra taken at zero backgates have first been analyzed because the

amplitude A and σ_I' in region I are not affected (or at least not considerably) by variations of V_g. Furthermore, the spectral weight of the exponential distribution is small or negligible at V_g = 0 V. Therefore, with variations of V_g, A and σ_I' have been fixed to the zero backgate values. Thus, the only fitting parameters when varying V_g are B and L_X. Moreover, we have analyzed up to 8 different directions for each PL image, obtaining a standard deviation for the transport length, typically ± 5 μm.

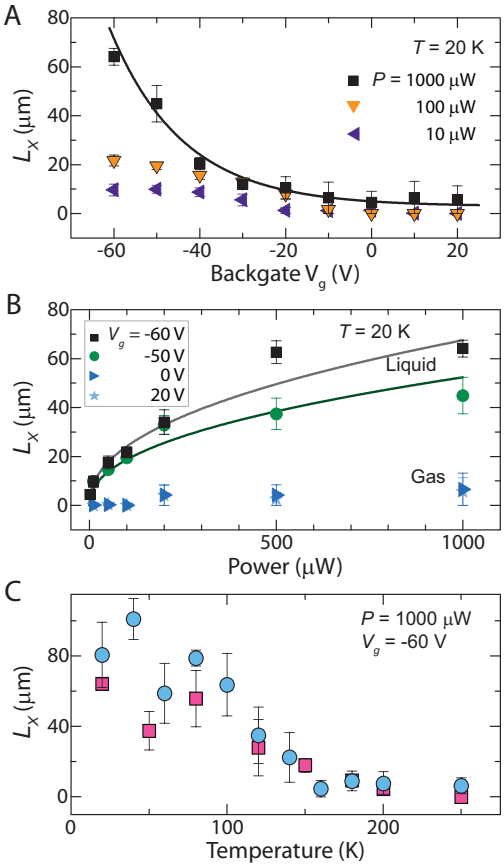

Fig. S8: Transport length analysis from PL cross-section analysis. (**A**) Transport length as a function of V_g for P = 1000 μW (black squares), 100 μW (down orange triangles) and 10 μW (horizontal blue triangles). The black solid line is an exponential fit to the data. (**B**) Power-dependence of L_X for V_g = -60 V (black squares), -50 V (green circles), 0 V (blue triangles) and +20 V (blue stars). In the liquid phase the data are well fitted by a square-root function of laser power. (**C**) Temperature-dependence of L_X reproduced in two devices. The curves have been obtained at fix V_g = -60 V and P = 1000 μW. In both samples, gas to liquid phase transition takes place at critical temperature of T_c $\sim$150 K.

B.2 Transport Length L_X: Parameters and Phase Diagrams From the bimodal analysis described in Section B.1, we obtain a comprehensive dependence of the transport length L_X on V_g, P and T, which is shown in Fig. 8 for each parameter. In Fig. 8(A), we clearly observe that L_X increases exponentially with decreasing V_g. For the highest used power (P = 1000 μW), L_X decreases from (64$\pm$3) μm to (5$\pm$4) μm. The same trend is observed for different powers. Figure 8(B) shows the power-dependence of L_X at several V_g. In the liquid phase at V_g = -60 V, we observe a sublinear increase of $L_X \propto P^{\delta}$ with the exponent of $\delta = (0.45 \pm 0.05)$ that is in excellent agreement with theory (see Section C below). Finally, we observe a decrease of L_X with increasing temperature, which have been reproduced among samples. L_X approaches to (5$\pm$4) μm at $T \geq T_c \approx 150$ K.

By using the values of L_X obtained from our analysis as a function of V_g, T and P, we construct the phase diagram $L_X(V_g, T)$ shown in Fig. 2(D) in the main text, and the phase diagram $L_X(V_g, P)$ at T = 20 K as shown in Fig. 9. Also in this diagram, we observe that the liquid phase emerges at negative backgate values, typically V_g = -30 V, even at the lowest excitation powers. Such a result manifest the absence of a threshold power for exciton condensation in monolayer MoS_2, which is in qualitative agreement with the theory [1] (see Section C below).

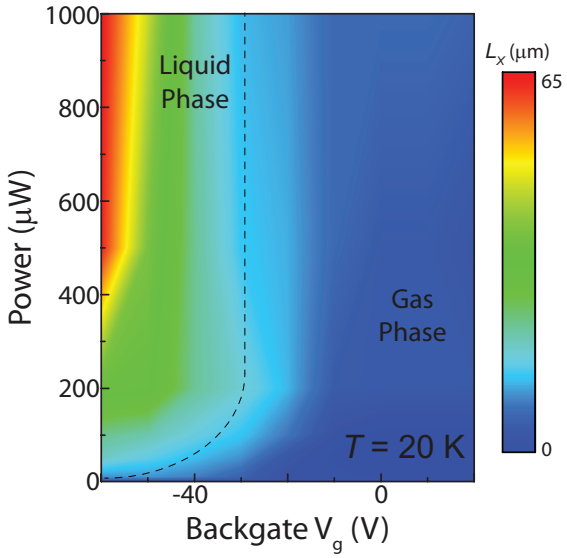

Fig. S9: Exciton phase diagram Phase diagram of the fluid transport length $L_X(V_g, P)$. The liquid (gas) phase domain, where the electron density is low (high), occupies the left-side (right-side) of the dashed guideline. The liquid phase emerges only at negative V_g regardless of laser power. The scale bar goes from 0 μm to 65 μm.

B.3 PL Intensity Analysis Similar to the enhancement of L_X, the strong brightening of the PL emission from the MoS_2 devices have a nonlinear dependence on V_g as the backgate voltage becomes more negative. Hence, the integrated PL intensity (I_{PL}) of the sample yield a similar parametric dependence as with L_X. The integrated PL intensity is measured by summing the intensity value at each pixel over the entire chip area defined by the sample geometry. For each PL image taken, the background noise, which manifests as a residual pixel value in the absence of photoexcitation is subtracted from the actual image.

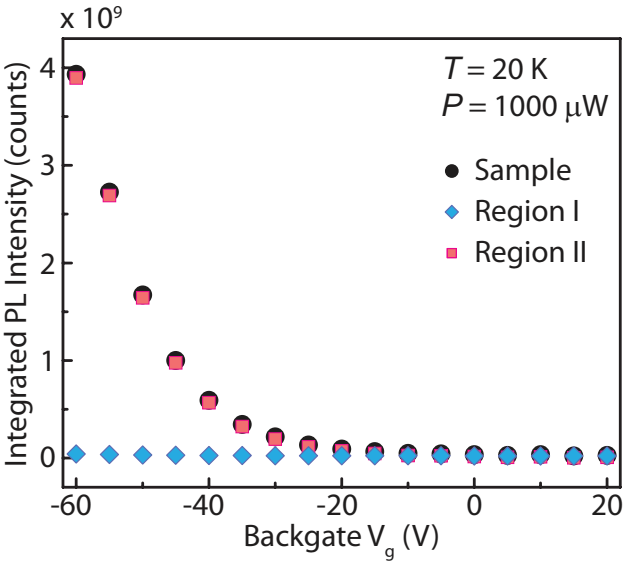

Fig. S10: Integrated PL intensity under regions I and II. The distribution of integrated PL intensity contributed by regions I (blue diamonds) and II (red squares) identified at 20 K for different V_g are compared with the total sample intensity (black circles).

In this way, we obtain the integrated PL intensity of the entire sample and of regions I (diffusive transport) and II (ballistic-like transport). The contributions to the integrated PL emission intensity by regions I and II, identified in the main text and Section B.1 as the laser excitation region and the spreading exciton density, respectively, are shown in Fig. 10. While the total integrated PL intensity increases (black circles), the PL from region I (blue diamonds) is roughly constant with V_g. Indeed, the PL superradiance arises from changes in region II (pink squares). When subjected to negative V_g, PL from region II dominates the integrated PL emission intensity and is two to three orders of magnitude more than

the PL emission in region I.

Compiling the values of I_{PL} in region II for different combinations of V_g, P and T, phase diagram using $I_{\mathrm{PL,II}}$ as the parameter have also been constructed as shown in Fig. 11, obtaining similar results than when using L_X as the characteristic macroscopic parameter to closely monitor the phase transition.

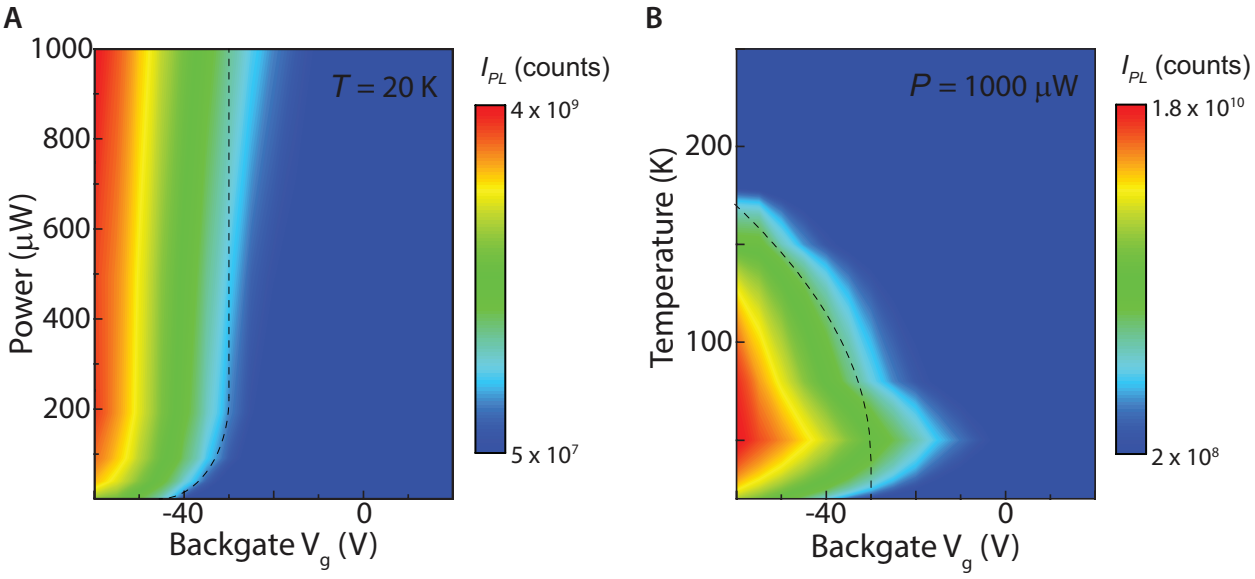

Fig. S11: PL intensity phase diagrams. Phase diagrams of the fluid light emission intensity **(A)** $I_{\mathrm{PL,II}}(V_g, P)$ at T = 20 K and **(B)** $I_{\mathrm{PL,II}}(V_g, T)$ at P = 1000 μW. The liquid (gas) phase domain, where the electron density is low (high), occupies the left-side (right-side) of the dashed guideline. The phase diagrams exhibit similar behaviour as when using the transport length L_X.

C. Exciton Condensation: Theory for Weakly Interacting Bosons Optical irradiation of a semiconductor generates a gas of electron hole pairs, which if bound via Coulomb attraction, form an exciton. At low densities, excitons are well described by Bose statistics. On contrary to the ideal case of atomic gases, exciton can interact via a potential $U(x)$, where x is the spatial separation among excitons, and depends on microscopic details of the photoexcited semiconductor. Therefore, considering interactions, the exciton Hamiltonian can be written as [2]:

$$H_X = \sum_k \left(E_X(0) + \frac{\hbar k_X^2}{2m_X^*} - \mu_X \right) a_{k_X}^\dagger a_{k_X} + \frac{1}{2\Omega} \sum_{k,k',q} U_q a\dagger_{k_X}^\dagger a_{k'_X} a_{k'_X+q} a_{k_X-q}, \quad (3)$$

where the first term correspond to the unperturbed exciton Hamiltonian $H_{\mathrm{o,X}}$ describing an exciton gas, while the second term $H_{\mathrm{Int,X}}$ describe exciton-exciton

interactions. If the potential is positive $i.e.$, $U(x) > 0$, it indicates repulsive interactions among excitons. a_{k_X} and $a\dagger_{k_X}$ are operators of creation and annihilation of particles, k_X is the exciton momentum, m_X^* is the effective exciton mass, E_g is the optical gap energy, μ_X is the exciton chemical potential and Ω is the volume of the system.

Spontaneously broken symmetry of the Hamiltonian is achieved by displacing the k_o term, which is equivalent to a transformation to the operators

$$\beta_o = a_o - \sqrt{\Omega n_o}\,; \beta_k = a_k \; if(k \neq k_o), \tag{4}$$

where n_o is the particle density. Since Ωn_o is a macroscopically large number, perturbation theory can be applied. The Hamiltonian is further simplified by means of a Bogoliubov transformation as

$$\xi_k = u_k \beta_{k+k_o} + v_k \beta^\dagger_{k-k_o}, \tag{5}$$

where u_k and v_k satisfy the relation $u_k^2 - v_k^2 = 1$ and each is given as

$$u_k = \sqrt{\frac{\frac{\hbar^2 k_X^2}{2m_X^*} + U_o n_o}{E(k)} + \frac{1}{2}}\;;\; v_k = \sqrt{\frac{\frac{\hbar^2 k_X^2}{2m_X^*} + U_o n_o}{E(k)} - \frac{1}{2}}. \tag{6}$$

where the spectrum of elementary excitations has the well-known form given by

$$E_{L,X}(k) = \sqrt{\left(\frac{\hbar^2 k_X^2}{2m_X^*}\right)^2 + \frac{U_o n_o \hbar^2 k_X^2}{2m_X^*}}. \tag{7}$$

In the case of repulsive interactions among excitons, the energy dispersion is modified by a linear term with k_X. Thus, in the limit of small wavevectors (or long-wavelengths) and sufficiently strong repulsions, the energy is governed by linear terms in k_X as $\lim_{k\to 0} E(k) \approx \sqrt{\frac{U_o n_o}{2m_X^*}}\hbar k_X = v_{L,X}\hbar k_X$, where the group velocity will be $v_g = \frac{\partial E_{L,X}(k_X)}{\hbar \partial k_X} \approx v_{L,X} \propto \sqrt{U_o n_o}$. Thus, it can be readily seen that for repulsive interactions ($U_o > 0$) will result in high propagation speeds and long transport lengths ($i.e.$, $L_X = v_{L,X}\tau_X$) of condensed excitons.

In a much detailed approach, Keldysh and Kozlov [1] have considered exciton-exciton, exciton-electron and exciton-hole interactions and calculate a more general expression for the velocity of condensed excitons given as

$$\Delta E_{X-X,L} = f\epsilon_b n_X a_B^2; \tag{8}$$

$$v_{X,L} = \sqrt{f\epsilon_b n_X a_B^2}, \tag{9}$$

where ϵ_b, n_X and a_B are the binding energy, the concentration and the Bohr radius of excitons, while the coefficient f represents the net interaction strength in the Bose and Fermi gas mixture. As discussed in the main text, f must take positive values for exciton condensation to take place. From Eq. (8)-(9), one can see that the repulsive interactions among excitons cause an energy shift of the exciton resonance, which scales linearly with the exciton density, and leads to high propagation speeds. For MoS_2 monolayer $f = f(V_g, T)$, thus the expression for the transport length L_X is as follows

$$L_X(V_g, T) = \sqrt{f(V_g, T)\epsilon_b n_X a_B^2}\, \tau_X. \tag{10}$$

One can see that for a fixed temperature and electron concentration ($i.e., V_g$), the transport length scales as $L_X \propto \sqrt{n_X}$, thus as a square-root of the excitation power, which is in excellent agreement with the experimental behaviour reported in Figures 8 and 9. Further calculations are required to obtain $f = f(V_g, T)$ for monolayer MoS_2.

C.1 Estimation of the critical temperature (T_c) as a function of intrinsic electron doping in monolayer MoS_2 Exciton condensation in monolayer MoS_2 takes place once the electron density n_e present in the two-dimensional semiconductor is equal or lower than the photogenerated exciton density n_X. Therefore, we assume that at charge neutrality the critical temperature (T_c) for exciton condensation is determined when an equal value of thermally activated electrons and photoexcited excitons are present in the monolayer ($i.e., n_e(T_c) = n_X(P)$).

We use a simple mass-action law model to estimate T_c as a function of the intrinsic two-dimensional electron density n_e^o. Furthermore, excitons can interact with free electrons to form negatively charge states or also called trions (X^-), whose density is n_{X^-}. The photoexcited electron density is $n_p = n_X + n_{X^-}$ and the electron doping density $n_d = n_e + n_{X^-}$ prior illumination. Thus, n_p and n_d can be controlled by an applied backgate voltage and light excitation power. To reach charge neutrality, the doping density n_e is controlled by the backgate, whose

density depends on V_g as

$$n_e = n_e^o + \frac{\epsilon_{\mathrm{r,SiO_2}} \cdot \epsilon_0 \cdot V_g}{d \cdot e}, \tag{11}$$

where ϵ_0 and $\epsilon_{\mathrm{r,SiO_2}}$ are the vacuum permittivity and dielectric constant of SiO_2 substrate underneath the monolayer. V_g is the applied backgate voltage. $d = 285$ nm is the thickness of the SiO_2 and e is the elementary charge. The density of generated excitons is calculated using the expression:

$$n_X = \frac{P}{E_{\mathrm{Laser}} A} \tau_X \cdot \alpha_X \cdot z_0 \cdot T_r, \tag{12}$$

where P is laser power, E_{Laser} is the laser energy, A is the laser excitation area (1.5×10^{-8} cm^{-2}), τ_X ($\sim$ 20 ps), α_X is the absorption coefficient at the exciton resonance (typically $\sim 10^5$ cm^{-1}), z_0 = 0.3 nm is the monolayer thickness and T_r (~ 0.9) is the transmission coefficient at the laser energy. Considering charge conservation,

$$n_p + n_d = n_X + 2n_{X^-} + n_e, \tag{13}$$

We solve Eq. (13) considering the rate equation $X + e \rightarrow X^-$ and the ratio $n_e(T)$ given by the mass-action law:

$$n_e(T) = \frac{4 M_X m_{\mathrm{e}}}{\pi \hbar^2 M_{X^-}} \cdot k_{\mathrm{B}} T \cdot e^{-\frac{E_{\mathrm{b}}}{k_{\mathrm{B}} T}}, \tag{14}$$

where $M_X \approx 2m_e$ and $M_{X^-} \approx 3m_e$ are the reduced mass of the neutral and negatively charge exciton, respectively, and $m_e = 0.5 m_o$ is the reduced mass of the electron with m_o the free electron mass. E_{b} is the trion binding energy, $\hbar$ and k_B are Planck and Boltzmann constants, respectively.

Solving the above set of equations at charge neutrality and for $n_X = 1.15 \times 10^{10}$ cm^{-2} (corresponding to the experimental condition P = 1000 μW), T_c is calculated and shown in Fig. 12 as a function of intrinsic electron concentration range characteristic of our devices, which at low temperatures is estimated as $n_e^o \approx [2.5 - 4.0] \times 10^{11}$ cm^{-2}. We observe that at low (high) intrinsic doping density n_e^o, T_c approaches 200 K (80 K). The monotonic behaviour suggest a minimal T_c of roughly 80 K. Furthermore, the fast increase at low n_e^o suggests that T_c could be pushed up to room temperature in ultraclean monolayer MoS_2, which could be achieved for instance by boron nitride encapsulation or by other dielectric engineering approaches.

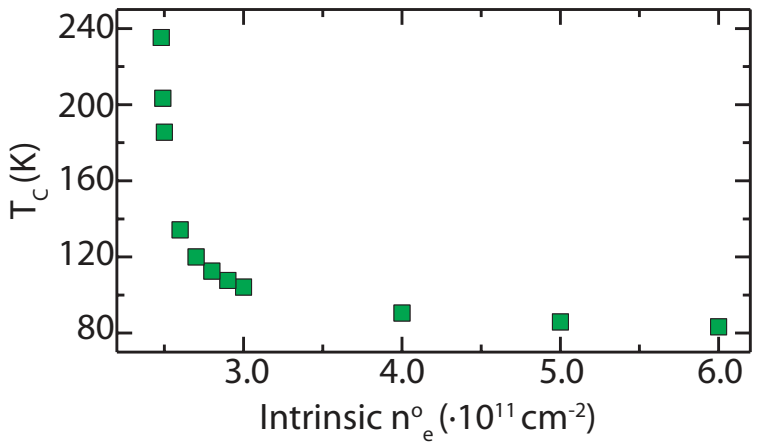

Fig. S12: Estimated Critical Temperature. Estimated temperature at which the thermally activated electron density n_e surpasses the exciton density $n_X = 1.15 \cdot 10^{10}\text{cm}^{-2}$.

D. Transient Reflectance Imaging of monolayer devices For each data set, we measured the dark noise image (D_{Noise}), laser background image (N_{BG}), as well as both pump-on (M_{On}) and pump-off (M_{Off}) reflectance spectrum map images. To obtain the differential reflectance (DR) images (R_{On} and R_{Off}) shown in the main text, the dark noise and laser background have been subtracted via the following expression:

$$R_{\text{On}}(x,E) = M_{\text{On}}(x,E) - N_{\text{BG}}(x,E). \quad (15)$$

$$R_{\text{Off}}(x,E) = M_{\text{Off}}(x,E) - D_{\text{Noise}}(x,E) \quad (16)$$

$$DR(x,E) = \frac{R_{\text{On}}(x,E) - R_{\text{Off}}(x,E)}{R_{\text{Off}}(x,E)}. \quad (17)$$

D.1 Analysis of ultrafast and non-linear transport of condensed excitons The energy flow associated with the spatial spreading of a photoexcited electronic density in a solid-state system gives rise to a typical transport behaviour. The type of transport that the population experiences can be determined by the temporal behaviour of the corresponding mean square displacement (MSD), which for a given spatial direction x is given by

$$\text{MSD} = \langle \Delta x(t)^2 \rangle = \langle x(t)^2 \rangle - \langle x(0)^2 \rangle = \kappa t^{\alpha}, \quad (18)$$

where κ is the transport coefficient, α is the anomalous exponent, $x(t)^2$ is the width of the spatial distribution of the population, with $x(0)^2$ the width at time

zero. A typical diffusive transport is described by $\alpha = 1$ and $\kappa = D$. When $\alpha \neq 1$, the transport is called non-diffusive or anomalous. For $0 < \alpha < 1$, the sublinear transport is denoted as sub-diffusive. For $1 < \alpha \leq 2$, the superlinear transport is denoted as super-diffusive. If $\alpha = 2$, transport is considered ballistic and $\kappa = v^2$ for propagation velocity v. From Eq. (18), the transport length L is defined over the lifetime τ of the photoexcited population, given by

$$L = \sqrt{\kappa \tau^{\alpha}}. \tag{19}$$

For classical diffusive transport, $L = \sqrt{D\tau}$, while for ballistic propagation $L = v\tau$. Multiple microscopy-based approaches exist to characterize the spatial spreading of a photoexcited excitonic density in a semiconductor. In steady-state measurements, the transport length L is obtained, while by using transient techniques, the exponent α ($i.e.$, type of anomalous propagation), κ and τ could be measured.

Based on the above considerations, we have analyzed the fwhm of the spatial cross section of the $DR(x, E_X(0))$ signal, evaluated at the exciton energy. The fwhm is denoted in the main text as σ_{II}. By obtaining the temporal evolution of $\sigma_{\mathrm{II}}(\Delta t)$, the type of transport can be identified. Fig. 13(A) shows a typical photobleaching cross-section at Δt = 1.2 ps extracted from the DR maps presented in the main text, taken at V_g = -60 V.

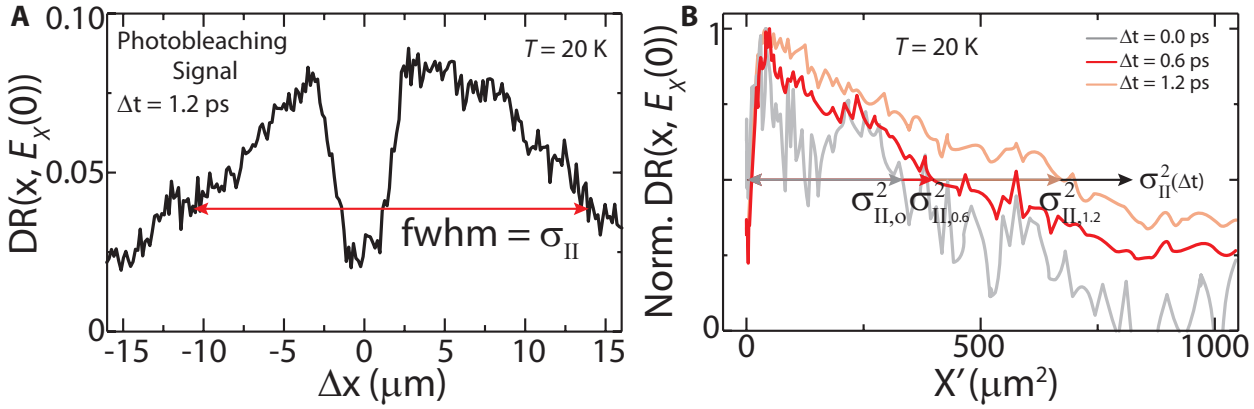

Fig. S13: Photobleaching Cross Section Analysis. (**A**) Background subtracted data showing photobleaching $DR(\Delta x, E_X(0))$ cross section taken Δt = 1.2 ps. (**B**) The averaged photobleaching signal $(DR(-\Delta x, E_X(0)) + DR(\Delta x, E_X(0)))/2$ as a function of $X' = 4\Delta x^2$ for Δt = 0 ps (gray line), 0.6 ps (red line) and 1.2 ps (orange line). The squared displacement $\sigma^2_{\mathrm{II}}(\Delta t)$ at each temporal frame is indicated.

We attribute the dip in the DR signal under the laser (Δx = (0$\pm$1) μm) to a fraction of excitons that remains in a non-interacting gas phase ($i.e.$, does not

form a liquid) due to the photo-induced charges (see section D.3 below). This is consistent with the bimodal PL distribution. Moving away from the excitation region, the DR signal increases and at the right side of the laser ($i.e.$, positive Δx values), it is constant from $\sim$ 2.5 μm until $\sim$ 8 μm, monotonically decreasing afterwards. The photobleaching signal exhibit an asymmetry at the left side of the laser ($i.e.$, negative Δx values), which we attribute to local disorder, microscopic ripples and dislocations, etc present in the monolayer. The asymmetric profile depends on the spatial slide of the monolayer selected in the experiments (by the spectrometer slit) and has been observed in several samples. At the time frame of 1.2 ps, the fwhm of excitonic fluid is $\sigma_{\rm II} \approx 25$ μm.

To accurately evaluate the displacement and to consider disorder of the sample, we have averaged the photobleaching signal at the right and the left-sides of the laser excitation. The obtained amplitude have been normalized to the maximum value and depicted as a function of the square of the spatial coordinate $X' = 4\Delta x^2$ (factor 4 appears when considering both sides of the laser). This procedure has been repeated for each temporal frame. Typical obtained curves are shown in Fig. 13(B) for several Δt. The obtained curves seem to follow a linear dependence with X' ($\propto 4\Delta x^2$), but having different slopes for different times resulting in the observed temporal progression of the photobleaching signal. At each temporal frame, $\sigma^2_{\rm II}(\Delta t)$ has been highlighted in Fig. 13(B) and is simply determined when the normalized DR = 0.5.

At $\Delta t = 0$ ps, the $\sigma^2_{\rm II}(0) = \sigma^2_{\rm II,o} = 325$ μm^2 is taken as reference to obtain the MSD defined as $\sigma^2_{\rm II}(\Delta t) - \sigma^2_{\rm II,o}$ which is presented in the main text. Fig. 14 depicts the ultrafast photoexcitation and condensation dynamics of excitons at V_g = -60 V. When Δt = -1 ps, no DR signal is detected. At Δt = -0.2 ps, we detect a positive signal at energy higher than the exciton resonance and is spatially distributed under the pump spot. The signal is attributed to the injected gas of excitons. This density undergoes rapid thermalization to the exciton resonance, where excitons condense, within 0.2 ps. After this nucleation period, propagation starts taking place.

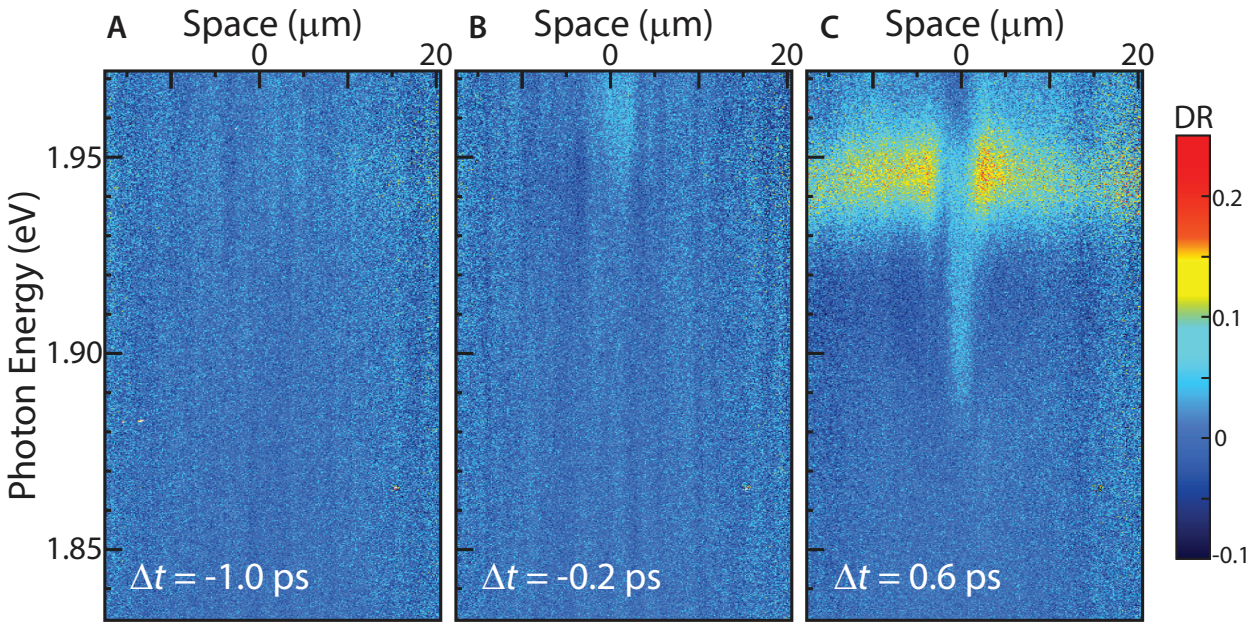

Fig. S14: Transport of condensed excitons: V_g = -60 V. Spatially- (horizontal-axis) and energy-resolved (vertical-axis) differential reflectance ($DR(x, E)$) at delay times (Δt) of (a) -1.0 ps, (b) -0.2 ps and (c) 0.6 ps.

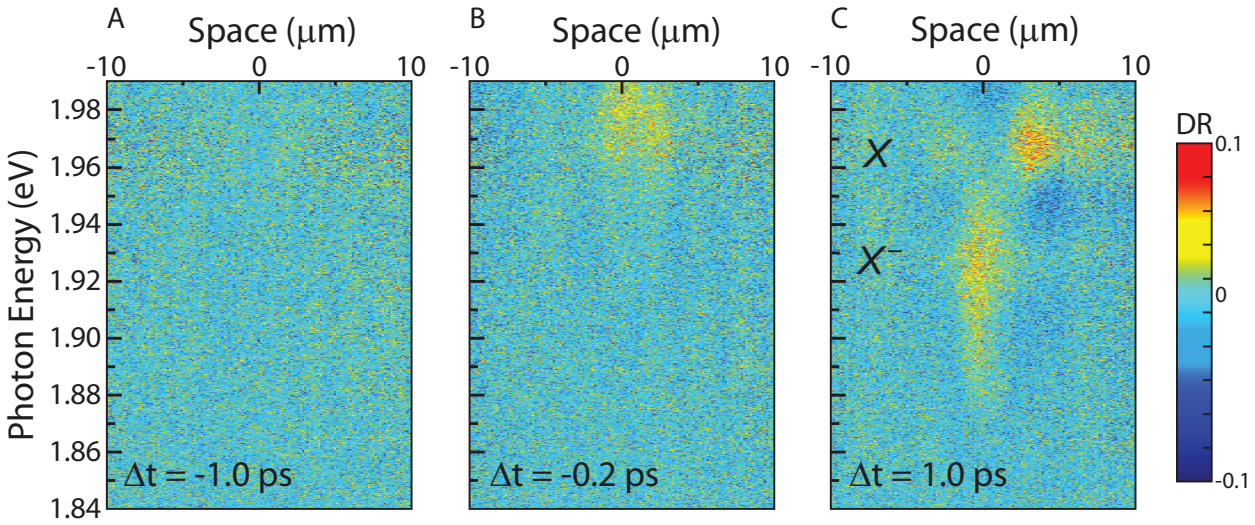

Fig. S15: Transport of (uncondensed) exciton gas: V_g = 0 V. Spatially- (horizontal-axis) and energy-resolved (vertical-axis) differential reflectance ($DR(x, E)$) at delay times (Δt) of (a) -1.0 ps, (b) -0.2 ps and (c) 1.0 ps.

We have also conducted differential reflectance experiments at V_g = 0 V to monitor the transport of excitons when in a weakly-interacting gas phase. Fig. 15 shows spatially- (horizontal-axis) and energy-resolved (vertical-axis) DR spectrum maps obtained for $V_g = 0$ V at different time delays. One can notice remark-

able differences on the propagation of excitons at the gas phase (Fig. 15(C)) as compared with excitons in the liquid phase (Fig. 14(C)).

At $V_g = 0V$, the positive feature undergoes a fast thermalization into the exciton resonance ($E_X(0) \approx 1.965$) and shows a maximum propagation of up to 5 μm, which is considerably smaller that the long-range propagation of condensed excitons. The temporal evolution of the MSD associated to photobleaching of the exciton gas has been presented in Fig. 4 of the main manuscript and exhibit a linear scaling law ($\mathrm{MSD_{Gas}} \propto \mathrm{t}$), indicative of diffusive transport. Finally, we notice that excitons decay into other states at lower energies whose transport length is comparable or smaller to the 5 μm of the exciton resonance.

D.2 Reproducibility of non-linear transport of condensed excitons The ultra-fast and long-range propagation of condensed excitons have been reproduced in two other devices as shown in Fig. 16. In these devices, similar lineshape and velocities have been obtained from the lineshape analysis of the photobleaching signal.

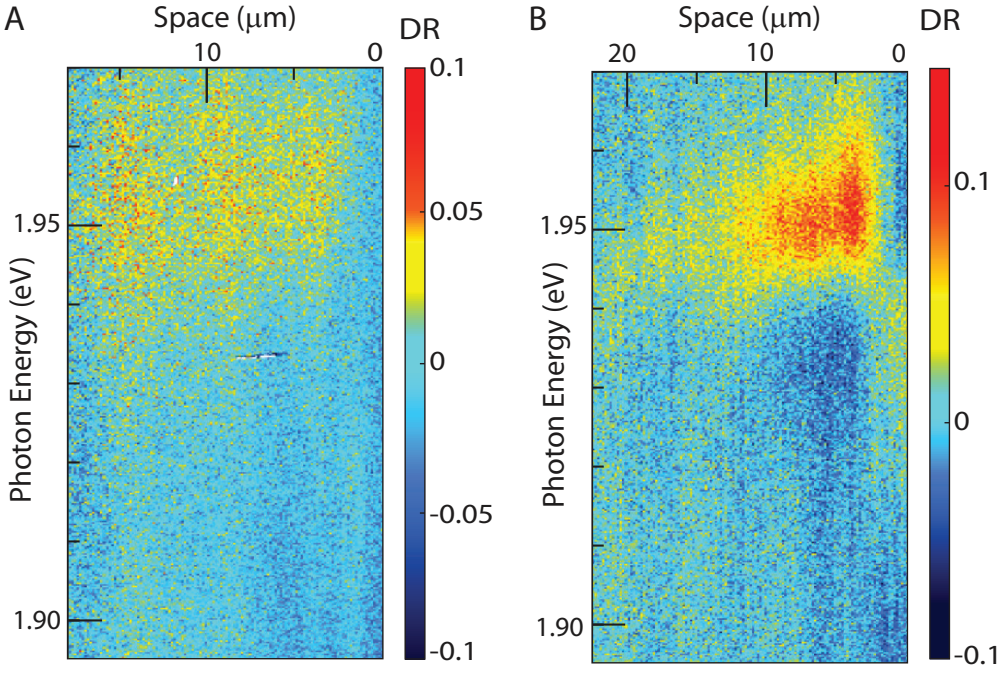

Fig. S16: Transport of condensed excitons in MoS_2 monolayer reproduced for two different devices at V_g = -60 V. Spatially- (horizontal-axis) and energy-resolved (vertical-axis) differential reflectance ($DR(x, E)$) at Δt = 2.0 ps obtained in two different devices.

D.3 Energy blueshift (repulsive interaction) of condensed excitons Signature of exciton condensation is the renormalization of the exciton resonance to higher energies due to the unconventionally strong many-body repulsive interactions present in the system as presented in Section C. At V_g = -60 V, a significant pump-induced blueshift of the exciton resonance is observed in Fig. 17 between pump-on (red curves) and pump-off (blue curves) raw reflectance data. The energy shift ($\Delta E_{\rm raw}$) is prominent and nearly constant in the range $\Delta x \in$[0-8]μm, coinciding with the onset of constant photobleaching amplitude in Fig. 14. $\Delta E_{\rm raw}$ decreases with increasing distance, coinciding with the decay of the photobleaching signal that is in agreement with Eq. (8).

The blueshift of the excitonic resonance can occur either by i) exciton-exciton repulsions or ii) upon variation on the dielectric environment of the excitons due to an increment on electron concentration. In main text Figure 4, we have distinguished the exciton-exciton repulsions from the blueshift due to doping. We have analyzed the lineshape of raw the reflectance data and obtain the spectral weight of neutral and charge excitons (or trions) in the reflectance data for pump-on and pump-off conditions. The relative weight of trions are presented in Figure 18(A) by blue circles and green squares for pump-on and pump-off conditions, respectively. The spectral weight of the trion resonance is proportional to the change in the doping concentration due to photo-induced charges.

We find that under pump on, the free carrier density increases to $\sim$35% nearby the laser spot and decrease fast with increasing distance to become negligible at $\Delta x \geq 6$ μm. The spatial profile of the trion suggests that charging follows the Gaussian distribution of the laser, and therefore, energy blueshift due to doping ($\Delta E_{\rm Doping}$) is important only nearby the laser. We notice a similar electron density under pump-on and pump-off conditions that suggests the small effect of photo-induced doping ($i.e,\ \Delta E_{\rm Doping}$) to the total energy ($\Delta E_{\rm Raw}$).

We quantify $\Delta E_{\rm Doping}$ by the expression given as

$$\Delta E_{\rm Doping} = m(b^{X^-}_{\rm On}(\Delta x) - b^{X^-}_{\rm Off}(\Delta x))n_{\rm Abs}, \tag{20}$$

where $b^{X^-}_{\rm On}(\Delta x)$ ($b^{X^-}_{\rm Off}(\Delta x)$) are the spatial profiles of the trion spectral weight presented in Fig. 18(A) for pump-on (pump-off) conditions. m = 3.18$\times 10^{-12}$ meV $\cdot$cm^2 is a constant obtained from the backgate dependence of the energy difference

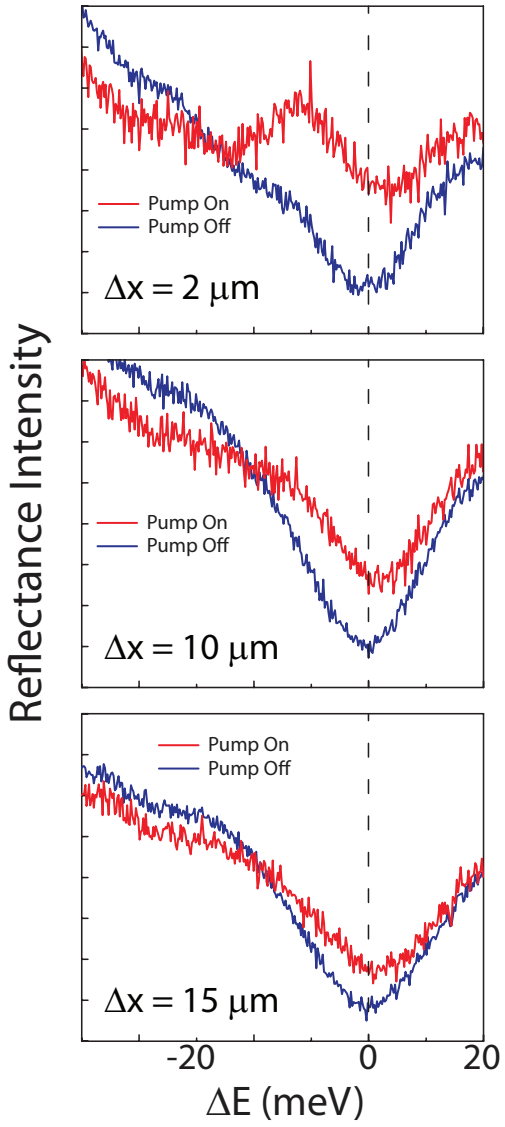

Fig. S17: Pump-induced exciton resonance blueshift. Reflectance spectra for Δt = 2.4 ps for pump-on (red curves) and pump-off (blue curves) conditions at Δx of (**A**) 2 μm, (**B**) 10 μm and (**C**) 15 μm. The data are plotted with respect to the exciton resonance energy for pump-off conditions.

between excitons and trions and quantify the changes in the exciton resonance upon an increase in electron density. The factor $n_{\mathrm{Abs}} \approx 2\times10^{12}$ cm^{-2} indicates the number of absorbed photons, calculated by using a monolayer thickness z_0 = 0.3 nm, absorption coefficient $\alpha_X = 10^5$ cm^{-1}, a pump fluence of up to 300 μJ/cm^2 at a wavelength of 615 nm and transmission coefficient of $T_r \sim 0.9$. Therefore, the estimated exciton gas density $n_X \approx 1.7\times10^{12}$ cm^{-2}, while the photo-induced change in the electron concentration by the pump is $\Delta n_{\mathrm{e,On}} \approx 2.5\times10^{11}$ cm^{-2}.

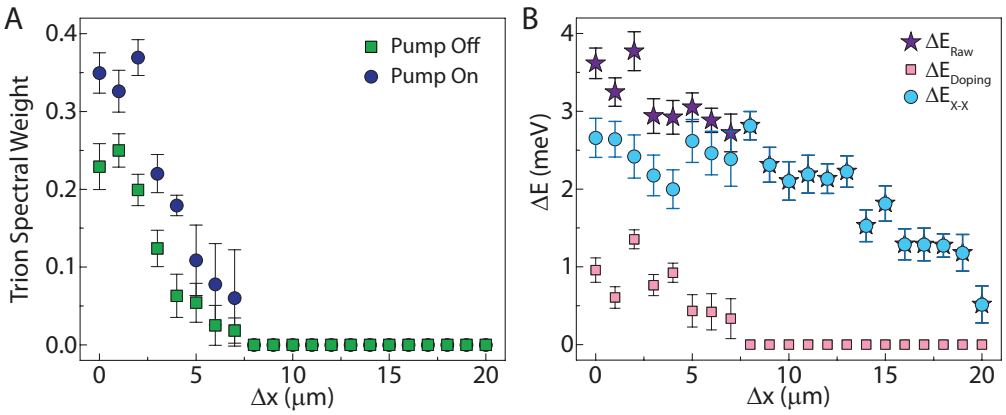

Fig. S18: Exciton blueshift due to many-body interactions. (**A**) Spatial dependence of the relative spectral weight of photoinduced trion population under pump-on (blue circles) and pump-off (green squares) conditions. (**B**) Spatial variation of the raw exciton energy difference ΔE_{Raw} (violet stars) and the corrected energy $\Delta E_{\mathrm{X-X}}$ (blue circles). The energy associated to photoinduced doping $\Delta E_{\mathrm{Doping}}$ is shown by pink squares.

The obtained spatial profile for the pump-induced doping $\Delta E_{\mathrm{Doping}}(\Delta x)$ is presented in Fig. 18(B). We find that $\Delta E_{\mathrm{Doping}}$ is up to at most $\sim$1 meV, which is lower than the raw difference ΔE_{Raw} = 3.7 meV (at Δx = 2 μm). The corrected blueshift given as $\Delta E_{\mathrm{X-X}} = \Delta E_{\mathrm{Raw}} - \Delta E_{\mathrm{Doping}}$, therefore, corresponds to the repulsive interaction energy between excitons (refer to main text Fig. 4B). As shown in Fig. 18, even for $\Delta x > 6$ μm where the photoinduced trion population is absent, the exciton resonance is still noticeably shifted to higher energies indicating the existence of a fraction of condensed excitons due to repulsive interactions among excitons.

1. Keldysh, L. V. & N., K. A. Collective properties of excitons in semiconductors. *Soviet Phsyics JETP* **27**, 978–993 (1968).

2. Moskakelnko, S. A. & W., S. D. Bose-einstein condensation of excitons and biexcitons and coherent nonlinear optics with excitons. *Cambridge University Press* (2000).